

AIRFIELD PAVEMENT RESPONSE DUE TO HEAVY AIRCRAFT TAKEOFF:
ADVANCED MODELING COMPARING SINGLE-TIRE AND DUAL-TANDEM GEAR

By:

Jaime A. Hernandez

PhD Candidate

Department of Civil and Environmental Engineering

University of Illinois at Urbana-Champaign

205 N Mathews Ave. MC-250, Urbana, IL 61801

Phone: 1 (217) 265-0427

Fax: 1 (217) 893-0601

E-mail: hrndzr2@illinois.edu

Imad L. Al-Qadi

Founder Professor of Engineering

Director, Illinois Center for Transportation

Department of Civil and Environmental Engineering

University of Illinois at Urbana-Champaign

205 N. Mathews Ave. MC-250, Urbana, IL 61801

Phone: 1 (217) 265-0427

Fax: 1 (217) 893-0601

E-mail: alqadi@illinois.edu

PRESENTED FOR THE
2014 FAA WORLDWIDE AIRPORT TECHNOLOGY TRANSFER CONFERENCE
Galloway, New Jersey, USA

August 2014

ABSTRACT

The normal and shear strains of a typical airfield pavement subjected to single and dual-in-tandem configuration of Airbus A380 were compared during takeoff. The contributions of this paper are threefold. First, a detailed description of the model generation and the process for including the variables usually omitted in typical pavement analysis are provided. These variables include variation of loading with time, nonlinear base materials, friction interaction between pavement layers, viscoelastic AC (asphalt concrete) layers, and three-dimensional nonuniform contact stresses. Second, the responses studied were not limited to the tensile strains at the bottom of AC layers and the maximum compressive strain on top of the subgrade, but also included the shear strains in each layer and surface tensile strain. Third, the comparison was not limited to magnitude as the variation of critical strains along the moving direction and its perpendicular was also considered, and the tire interaction in the dual-in-tandem configuration was described.

INTRODUCTION

The current pavement design methodology recommended by Federal Aviation Administration (FAA) [1] is based on assumptions misrepresenting the actual characteristics of flexible pavements. First, all material are assumed to be linear elastic, even though asphalt concrete is viscoelastic, and granular materials are nonlinear. Second, the load is assumed to have uniform magnitude and act vertically on a circular area, but stresses transferred by pneumatic tires to pavement are three-dimensional, nonuniform, and act on a contact area that depends on the tire geometry. Finally, the ability of the current design method to consider gear interaction is limited.

The most relevant effort to experimentally quantify the impact of multiple wheels on the response of airfield pavement was sponsored by the National Airport Pavement Test Facility (NAPTF) [2]. NAPTF is a full scale accelerated pavement loading site specialized in airfield pavements and capable of simulating full landing gears with a maximum wheel load of 334 kN and a maximum aircraft weight of 5783 kN. Construction cycles have been conducted at NAPTF, providing valuable insight into the impact of multiple wheels on stresses, strain, and deflections of flexible airfield pavements.

The first construction cycle (CC1) was composed by six flexible pavement sections built on three subgrades ($CBR = 3, 8, \text{ and } 20\%$). The sections were used by Gomez-Ramirez and Thompson [3] to determine wheel load interaction and by Thompson and Garg [4] to validate an analytical procedure to account for such interaction using experimental measurements (multi-depth deflectometers and pressure cells data) from CC1. Low-strength subgrade allowed higher wheel interaction for deflection, and the degree of interaction decreased as the subgrade strength increased. In addition, such interaction was higher when switching from dual to dual-tandem than from dual-tandem to dual-tridem. It was also observed that the effect of multiple wheels on deflection was greater than their effect on stresses. Gopalakrishnan and Thompson [5, 6] measured a similar rut depth for dual-tridem and dual-tandem loading configurations in CC1 and conducted a close number of repetitions to reach 25.4-mm rut depth.

Based on numerical analysis, Kim and Tutumluer [7] showed that the results of multiple axles based on superposition of single axle responses were conservative, except for the subgrade vertical strains on thin pavements. Using this modeling approach, the influence of multiple wheels was observed not only on the values of critical pavement responses but also on their locations. In addition, Zhao et. al [8] found that the difference between single wheel and full landing gear increased with the increase in pavement stiffness, and the surface deflection and vertical strain on top of the subgrade were the most affected.

This study used advanced three-dimensional finite element model that considered viscoelastic asphalt layers [9], nonlinear granular materials [10, 11], and three-dimensional dynamic nonuniform contact stresses [12-15] with appropriate variation with time [14, 16] to study the effect that tire inflation pressure and gear configuration have on the responses of airfield pavements. The variation of the responses along perpendicular directions in the plan view was also studied.

The main objective of this study is to assess the impact of dual-tandem wheel configuration on critical pavement responses. This document was divided in two parts. First, relevant components of the finite element model are detailed, including dimensions of the model, mesh configuration, wheel configurations and loading conditions, material characterization, and boundary conditions. The second part focuses on the variation of pavement responses along the moving direction and its perpendicular and on a comparison between the impact of single and dual-tandem wheel configurations.

FINITE ELEMENT MODEL

A three-dimensional finite element (FE) analysis of an airfield pavement structure built at the NAPTF and part of the Boeing high tire pressure test program was performed using Abaqus [15]. The structure was subjected to A380's landing gear in addition to a single wheel of the configuration. The tire was assumed to be inflated at two levels: 1.45 and 1.69 MPa. The advanced FE model considered variables omitted in the conventional analysis of flexible pavements such as viscoelastic asphalt materials, nonlinear granular materials, and three-dimensional nonuniform contact stresses. The analyzed pavement structure consisted of 125 mm of hot-mix asphalt (HMA) (P-401), 200 mm of crushed stone (P-209), 150 mm of Econocrete (P-306), and 810 mm of uncrushed stone (P-154). A detailed description of the model definition including geometry, mesh configuration, loading, and material characterization is provided in the following section.

Geometry and Mesh Configuration

The model dimensions were defined in plan and profile view by comparing the responses of a simplified finite element model and BISAR, linear elastic pavement analysis software. The optimum FE model configuration, including number and type of elements, resulted from the responses with the smallest difference between Abaqus and BISAR when considering the same material characteristics and loading conditions.

The model dimensions in plan view are shown in Figure 1. The length and width of the model and loaded area are L , B , X , and b , respectively. The loading area contained relatively small elements while the boundaries included relatively large elements. Distances $L1$, $L2$, $B1$, and $B2$ were used to provide a smooth transition from small elements in the loading area to the boundaries of the model. All dimensions were optimized during the mesh sensitivity analysis.

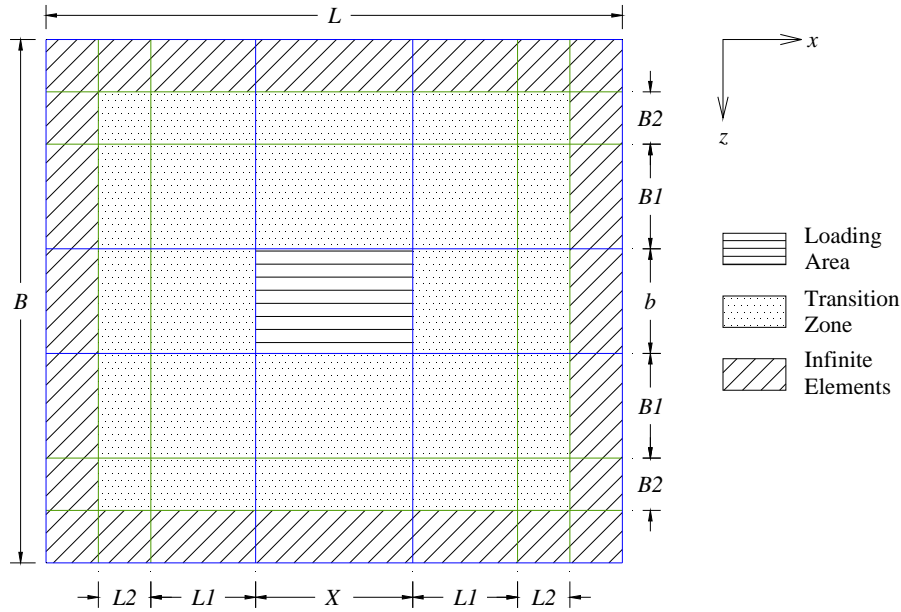


Figure 1. Model dimensions in plan view.

A mesh sensitivity analysis was performed by changing the size of finite elements until the difference in the results between a simplified FE model and BISAR was insignificant. The small finite elements decreased the difference, but increased the running time, which is significant when performing three-dimensional analysis. Infinite elements were used [17] to efficiently represent the decay of pavement responses in the boundary of the model. The final location and length of the infinite elements were part of the outcome of the mesh sensitivity analysis.

The simplified pavement model used in the mesh sensitivity analysis assumed fully bonded linear elastic layers with circular contact area and uniform contact stresses in the vertical direction only. A contact pressure of 1.5 MPa was applied on a circular contact area of radius 240.0 mm. The elastic moduli of each layer used in the simplified model are presented in Table 1. The table also shows the number of elements in each layer N , the bias ratio (ratio of the first and the last element length along each layer's thickness), and the length of the first and last element in each layer. It was also found that $L1 = B1 = 3000$ mm (15 elements with bias factor of 20) and $L2 = B2 = 300$ mm (one element). The final length of the infinite elements in the boundary of the model was 500 mm.

The values in Table 1 were found by comparing the tensile strain at the bottom of the AC $\varepsilon_{11,ac}$, the vertical strain on top of the subgrade $\varepsilon_{22,sg}$, and the maximum shear strain in each layer. The highest difference for the tensile strain was observed at the bottom of the AC at 2200 mm away from the load center ($2.5 \mu\varepsilon$). The difference in most values was in the range of 5%.

Table 1. Elastic Moduli and Mesh Size in each Layer

| Layer | Thickness (mm) | E (MPa) | N | Bias | 1st Element (mm) | Last Element (mm) |
|-------------------------|----------------|---------|----|------|------------------|-------------------|
| AC (P-401) | 125.0 | 3151.0 | 20 | 1.5 | 5.1 | 7.6 |
| Base (P-209) | 200.0 | 518.0 | 20 | 1.5 | 8.1 | 12.2 |
| Econocrete (P-306) | 150.0 | 4830.0 | 10 | 1.5 | 12.1 | 18.2 |
| Uncrushed Stone (P-154) | 810.0 | 276.0 | 30 | 1.5 | 21.9 | 32.8 |
| Subgrade | 4715.0 | 36.0 | 20 | 1.5 | 35.9 | 718.5 |

Loading

Pavement loading was fully defined by specifying three characteristics: Tire-pavement contact area; distribution and magnitude of 3D contact stresses; and variation of contact stresses with time. Two values of tire inflation pressure were assumed, $\sigma_o = 1.45$ and 1.69 MPa. Each value of tire inflation pressure affected the distribution of contact stresses, but it was assumed that the values did not modify the contact area or the variation of loading with time.

Two gear configurations of Airbus A380 landing wing were considered: single *S* and dual-in-tandem *2D*. The longitudinal and transverse center-to-center distances were 1700 and 1350 mm, respectively. These values were obtained from the aircraft's specifications published by the manufacturer [18]. As reported by Wang and Al-Qadi [15], each tire was assumed to be composed of five 560-mm-long ribs. The width of Ribs 1 and 5, Ribs 2 and 4, and Rib 3 were 70, 40, and 90 mm, respectively, as shown in Figure 2. The groove was 10 mm.

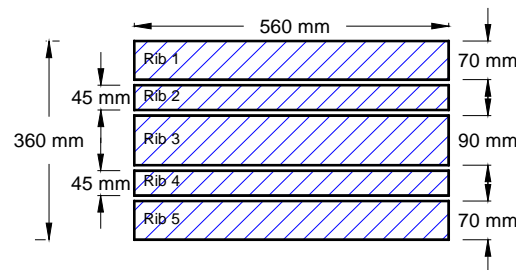


Figure 2. Contact patch details.

Contact Stresses Distribution

Three-dimensional nonuniform contact stresses were considered based on the results reported in the literature [19]. The shape of the vertical and transverse contact stresses was assumed to be the same, with the only difference in the magnitude of its peak values. On the other hand, the longitudinal contact stresses were given by two consecutive skewed parabolas. The vertical contact stresses for one rib were as follows:

$$\sigma_z(z) = \frac{\alpha P}{lb} \left(1 + \frac{1}{2n}\right) \left[1 - \left(2\frac{x}{l} - 1\right)^{2n}\right] \quad (1)$$

where: P = applied tire load

l = contact length

b = rib's width

x = distance along contact length

α = percentage of applied load carried by the rib ($\alpha = 0.28$ for Rib 1 and 5; 0.11 for Rib 2 and 4, and 0.22 for Rib 3)

n = parameters defining the shape of the variation

Assuming that the maximum contact stresses occurs at the contact length's midpoint, n can be computed as:

$$n = \frac{1}{2 \left(\frac{lb\sigma_{max}}{\alpha P} - 1 \right)} \quad (2)$$

where $\sigma_{max} = 1.1$ times the tire inflation pressure for Rib 2, 3, and 4 and 1.8 times the tire inflation pressure for Rib 1 and 5. The shape of the transverse contact stresses was the same as $\sigma_z(x)$, but with 40% of the magnitude.

Finally, the longitudinal contact stresses $\sigma_x(x)$ were defined by two skewed parabolas having a positive peak of magnitude $\sigma_x = 0.20\sigma_{max}$ at $x = 0.2l$ and a negative peak of $\sigma_x = -0.15\sigma_{max}$ at $x = 0.85l$. The general expression for a skewed parabola is $y = a_3xy + a_2x^2 + a_1x + a_0$, where a_1 , a_2 , a_3 , and a_4 are constants that can be found from continuity, maxima, and zero-value conditions. The equation for σ_x in MPa as a function of x in mm can be calculated as follows:

$$\frac{\sigma_x}{\sigma_o} = \frac{-1.594 \times 10^{-5}x^2 + 5.36 \times 10^{-3}x}{1 + 8.93 \times 10^{-3}x} \quad \text{if } 0 \leq x \leq 0.60l \quad (3)$$

$$\frac{\sigma_x}{\sigma_o} = \frac{3.905 \times 10^{-6}x^2 + 3.50 \times 10^{-3}x + 0.735}{1 - 1.46 \times 10^{-3}x} \quad \text{if } 0.60l \leq x \leq l \quad (4)$$

The variation of $\sigma_x(x)$, $\sigma_y(x)$, and $\sigma_z(x)$ along the contact length for rib 1 and 5 and both inflation pressures are presented in Figure 3.

To simulate the pavement response during takeoff, which is composed of 14 time increments, the variation of the load applied was divided into two stages. In the first stage, from increment 1 to increment 7, the elements in the tire's footprint were gradually loaded as the wheel approached the loaded region. In the second stage, from increment 8 to increment 14, the elements were suddenly unloaded (takeoff). The duration of each increment depended on the traveling speed, which was assumed to be 340.0 km/h.

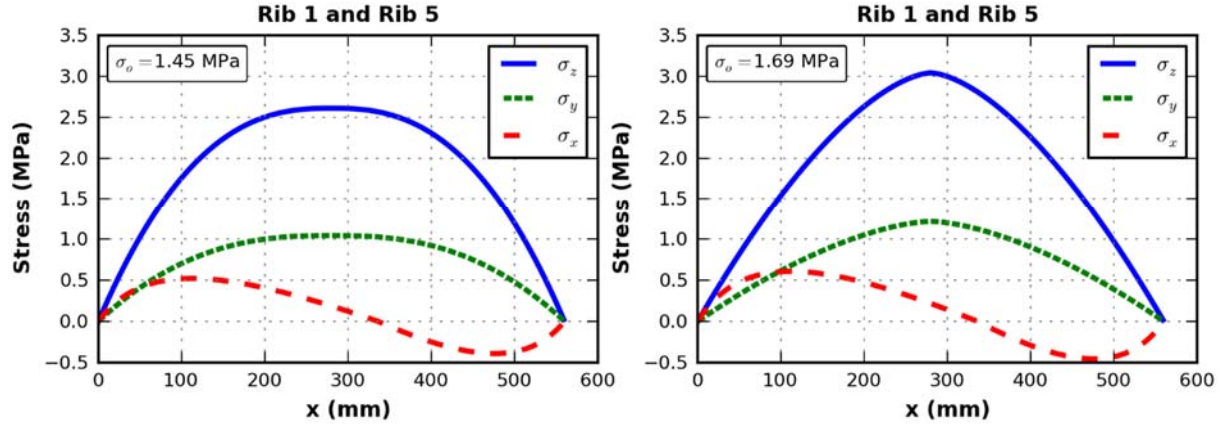


Figure 3. Nonuniform contact stresses in three directions for Rib 1 and 5.

Figure 4 graphically describes the mentioned process for one wheel in the gear configuration. In the first stage, the load was moved 80 mm in each increment, the equivalent of four finite elements, which implies the need for seven increments for the load to cover the contact length (560 mm). As observed in the figure, during increment 1, the elements in the first 80 mm were loaded and, during increment 2, the elements up to 160 mm were loaded. The procedure was repeated until all the elements were loaded (increment 7). The transition from one increment to the next was not sudden. On the contrary, the linear variation of the contact stresses was considered with time as they changed their position [14]. This linear variation was defined by the magnitude of the stresses in the current and next increment and the time needed by the tire to move 80 mm. During the second stage (takeoff), the elements were suddenly unloaded. The elements in the footprint were unloaded between increments 8 and 14, and the amplitude of the contact stresses was decreased following the descending portion of the Haversine function. Stage 2 ended in increment 14 when all elements were fully unloaded and takeoff was completed.

Figure 5 shows a sample of the amplitude of the contact stresses for three representative elements in the tire-pavement contact patch: Beginning, middle, and end of contact area. In the plot, the transition between stage 1 (load approach) and stage 2 (takeoff) occurred at $t = 8.4$ ms. In other words, $t = 8.4$ ms was the time needed by the load to travel the contact length. If the element was located at the beginning of the contact area, it felt the load in the first increment. This is the reason for its amplitude being zero only at $t = 0.0$ ms. As the load passed the element, the amplitude increased until the center of the stress distribution passed the element (where the

stresses were maximum). After reaching the peak, the amplitude started to decrease. If the element was in the middle of the contact length, a few milliseconds (3.6 ms in this case) were needed for the load to reach this element. Afterward, the amplitude increased in linear segments of different slopes. Finally, the element at the end of the contact patch was loaded during the last increment of stage 1. After the contact area was loaded, the amplitude was the same for all elements given by sudden unloading defined by descending portion of Haversine pulse.

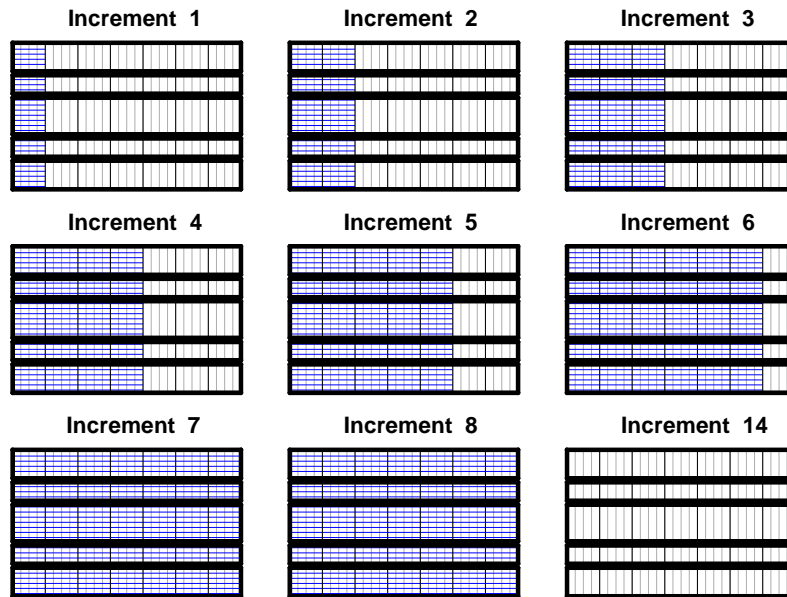


Figure 4. Variation of loaded elements with time.

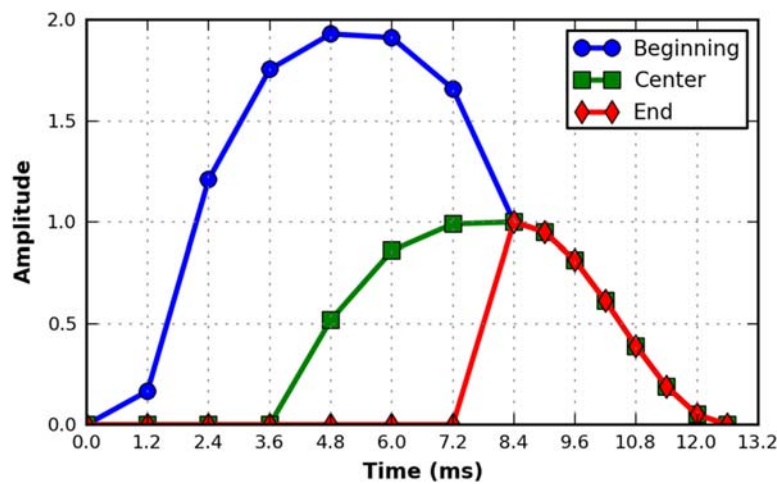


Figure 5. Amplitudes for representative elements in contact area.

Materials Characterization

In the case of AC, linear viscoelasticity was used based on dynamic modulus test results. The master curve was built by shifting E^* to a reference temperature of 21°C. In the case of granular layer with high stress level, the nonlinear (isotropic stress-dependent) model was used. Resilient modulus test results for crushed (P-209) are available at the NAPTF web site [2]. The rest of the layers were considered as linear elastic with properties presented in a previous study [15].

Boundary Conditions

Three-dimensional and plan view of the finite element model are presented in Figure 6. Infinite elements were assigned on the outer boundary of the model in the horizontal and vertical directions. No degrees of freedom were restrained in the horizontal direction; however, translation in the three principal directions were prevented at the bottom of the subgrade. Aforementioned loaded area, transition zone, and infinite boundary can be clearly seen in Figure 6.

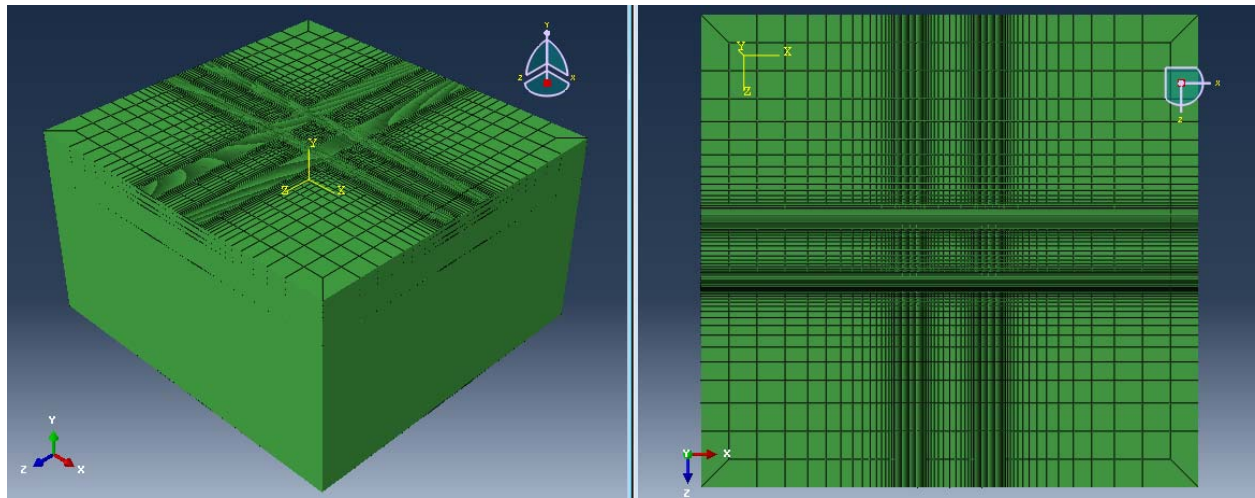


Figure 6. 3D and plan view of FE model for dual-tandem gear configuration.

RESULTS AND ANALYSIS

Even though the current design procedure of FAA only considers the tensile strain at the bottom of the AC ($\epsilon_{11,ac}$ and $\epsilon_{33,ac}$) and vertical strain on top of the subgrade ($\epsilon_{22,sg}$), responses linked to top-down cracking and permanent deformation were also studied [transverse surface strain ($\epsilon_{33,sf}$) and vertical shear strain in each layer (AC: $\epsilon_{23,ac}$, base: $\epsilon_{23,bs}$, subbase: $\epsilon_{23,sb}$, and subgrade: $\epsilon_{23,sg}$)]. Vertical shear strain ϵ_{13} was not analyzed because the maximum values occurred ahead of the tire in a highly compressed zone, where cracking is less likely to happen.

Table 2 compares critical pavement responses following the assumptions of conventional pavement analysis (WinJULEA), and 3D finite element analysis from this study. The difference between both methods varied widely. For instance, in the case of tensile strain at the bottom of the AC in the longitudinal and transverse direction, conventional analysis provided unsafe result from the pavement design perspective. Conversely, for ϵ_{23} in the base and the subgrade, calculations from 3D FEM provided smaller results, indicating WinJULEA overestimated the responses, which would result in an expensive design. Finally, for the shear strain in AC and vertical strain on top of the subgrade, outcomes were in good agreement. Not only magnitude but also location varied with respect the method used. Using conventional analysis, maximum ϵ_{22} in the base occurred on top of the layer. Conversely, considering the stress-dependency of resilient modulus changed the location to the middle of the layer. The observations and conclusions from this comparison are applicable to the particular case described, and they should not be generalized to other pavement structure and loading conditions.

Table 2 Comparison of Critical Responses from WinJULEA and 3D FE Model

| | WinJULEA | 3D FEM | Diff. (%) |
|--------------------|----------|--------|--------------|
| $\epsilon_{11,ac}$ | 377.8 | 480.2 | 27.1 |
| $\epsilon_{33,ac}$ | 377.8 | 495.3 | 31.1 |
| $\epsilon_{22,bs}$ | 1893.7 | 3052.8 | 61.2 |
| $\epsilon_{22,sg}$ | 547.9 | 557.0 | 1.7 |
| $\epsilon_{23,ac}$ | 196.5 | 200.1 | 1.8 |
| $\epsilon_{23,bs}$ | 734.4 | 350.3 | -52.3 |
| $\epsilon_{23,sg}$ | 189.6 | 108.5 | -42.8 |

Figure 7 presents the critical normal and shear strains for both gear configurations (S and $2T$) and tire inflation pressures ($P1$ and $P2$). The most affected strain by the gear configuration was $\epsilon_{33,sf}$, which doubled after changing from single tire to dual-in-tandem. In addition, $\epsilon_{23,bs}$ and $\epsilon_{23,sg}$ increased 15 and 35%, respectively. Tire inflation pressure also affected some critical strains, but not as significantly as gear configuration. The greatest change was observed for $\epsilon_{11,ac}$ and $\epsilon_{23,ac}$, which was approximately 10%.

To better understand the effect of gear configuration and tire inflation pressure, the variation of normal and shear strains were carefully studied along the moving direction (X) and its perpendicular (Z). Figure 8 and Figure 9 show the variation of $\epsilon_{11,ac}$, $\epsilon_{33,ac}$, $\epsilon_{22,sg}$ and $\epsilon_{33,sf}$ along X and Z , respectively. The longitudinal strain at the bottom of the AC was always in tension along Z . Each peak corresponded to a tire location (1 for S and 2 for $2D$), and its magnitude was more affected by P than by the gear configuration. For the dual-in-tandem, the strain decreased with the increase in the distance from the tire, but it did not fully reach zero between the tire (the minimum values was $\epsilon_{11,ac} = 143.4 \mu\epsilon$). This indicates some degree of interaction between both tires in the transverse direction. In the longitudinal direction, the strain presented as many peaks as tires in the configuration with very similar magnitude. However, compressive longitudinal strains were observed before and after each positive peak. The

behavior of $\varepsilon_{33,ac}$ was reserved when compared with $\varepsilon_{11,ac}$: and the change along Z showed small compressive peaks before and after the maximum tensile strain which was always positive in the X direction.

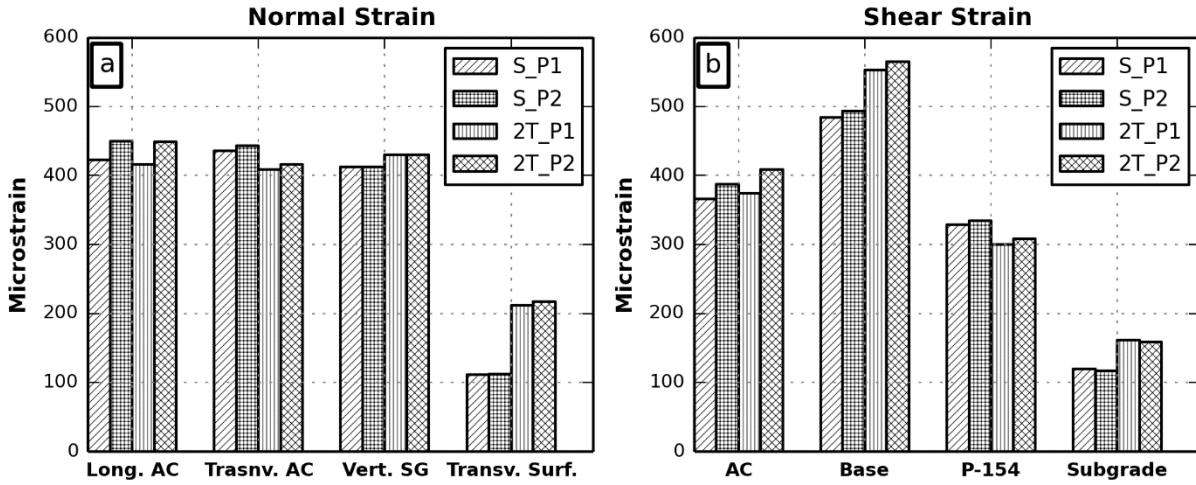


Figure 7. Effect of gear configuration and inflation pressure on pavement responses.

As expected, the vertical strain on top of the subgrade was compressive for all the range of values in the X and Z directions. The strain at the valley between the tires in the $2D$ configuration was significantly higher in the Z than in the X direction (391.7 vs. $249.8 \mu\epsilon$). This variation was attributed to the fact that the distance was shorter between the tires in the transverse direction than in the longitudinal one.

The high interaction between the tires was observed in the gear configuration for $\varepsilon_{33,sf}$. Along the X direction, the strain was always positive. The variation in the transverse direction showed a highly compressed zone in the region under the tire and its immediate vicinity. This highly compressed zone was followed by a peak tensile strain at both sides of the tire. For the $2D$ configuration, the positive peaks of each tire were superimposed, creating a tensile strain twice the magnitude corresponding to the single tire configuration.

Figure 10 and Figure 11 show the variation of the vertical shear strain in each layer $\varepsilon_{23,ac}$, $\varepsilon_{23,bs}$, $\varepsilon_{23,sb}$, and $\varepsilon_{23,sg}$ along the X and Z directions. The behavior along the two directions was very similar in each layer, and the only difference observed was the magnitude of the peaks. Along the moving direction, the shear strain did not change sign, and clearly defined peaks according to the number of tires were observed. For the perpendicular direction, the shear strain changed its sign while crossing the region underneath the tire. For the single-tire configuration, the magnitude of the critical ε_{23} was the same at both sides of the tire for every layer. This was also the case for the dual-tandem configuration when the outermost peaks were compared.

Shear strains were more affected by gear configuration than normal strains, and the gear interaction became more relevant as depth increased. In the X direction, for instance, the ratio of shear strain in the valley between the two peaks and the peak magnitude in the AC was 0.03, but it gradually increased to 0.04, 0.36, and 0.63 in the base, subbase, and subgrade, respectively. Another evidence of this behavior is the ratio between magnitudes of peak shear strains closest to one tire along the Z direction. In the AC, this ratio was 1; however, in the base, subbase, and subgrade it changed to 0.80, 0.56, and 0.07, respectively.

CONCLUSIONS

Advanced finite element modeling was used to assess the effect of gear configuration and tire inflation pressure on critical pavement responses. These critical pavement responses included tensile strain at the bottom of the AC, surface tensile strain, and a vertical strain at the bottom of the AC. In addition, a vertical shear strain was studied in each layer. A detailed description of the model definition was provided along with variation of critical strain along main directions in the model. The results showed the major influence of gear configuration on tensile transverse surface strain and shear strain in the base and the subgrade. The tire inflation pressure did not greatly affect the studied pavement responses deep in the pavement. These influences were verified by analyzing the variation of each responses along the principal directions of the model.

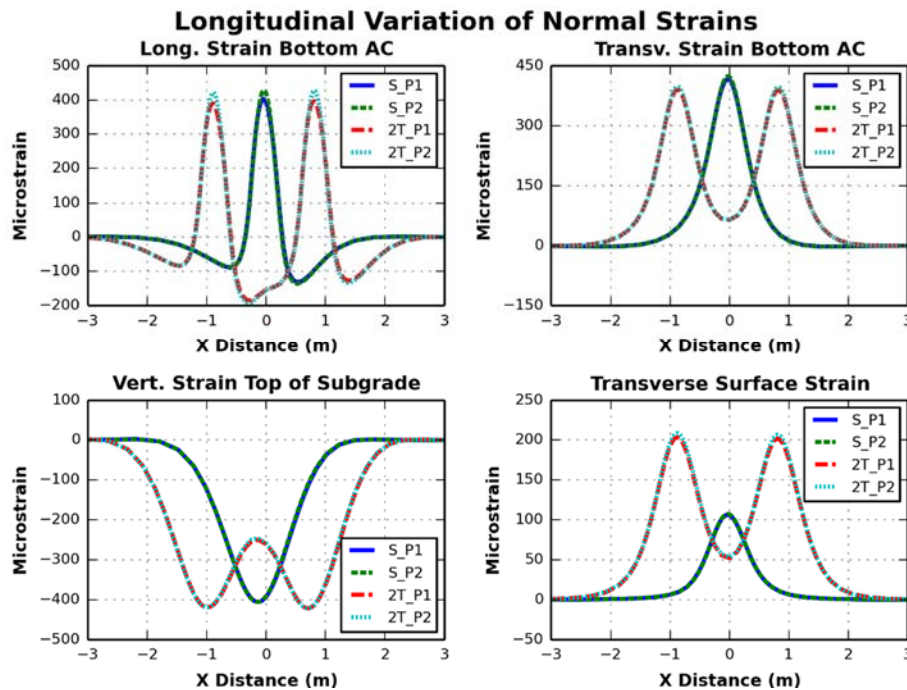


Figure 8. Variation of normal strains along the direction of traffic.

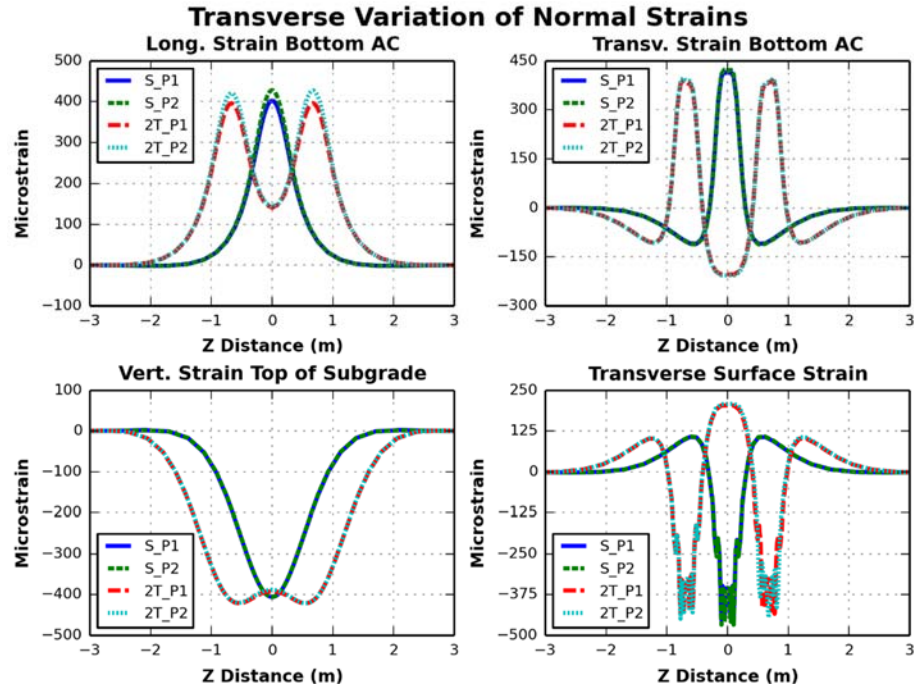


Figure 9. Variation of normal strains along the direction perpendicular to traffic.

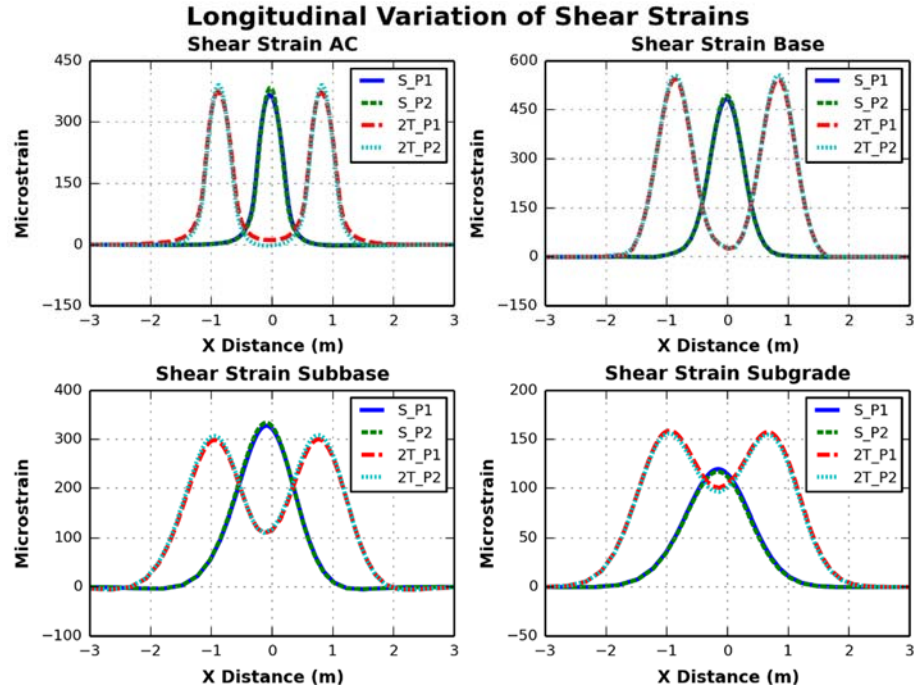


Figure 10. Variation of shear strains along the direction of traffic.

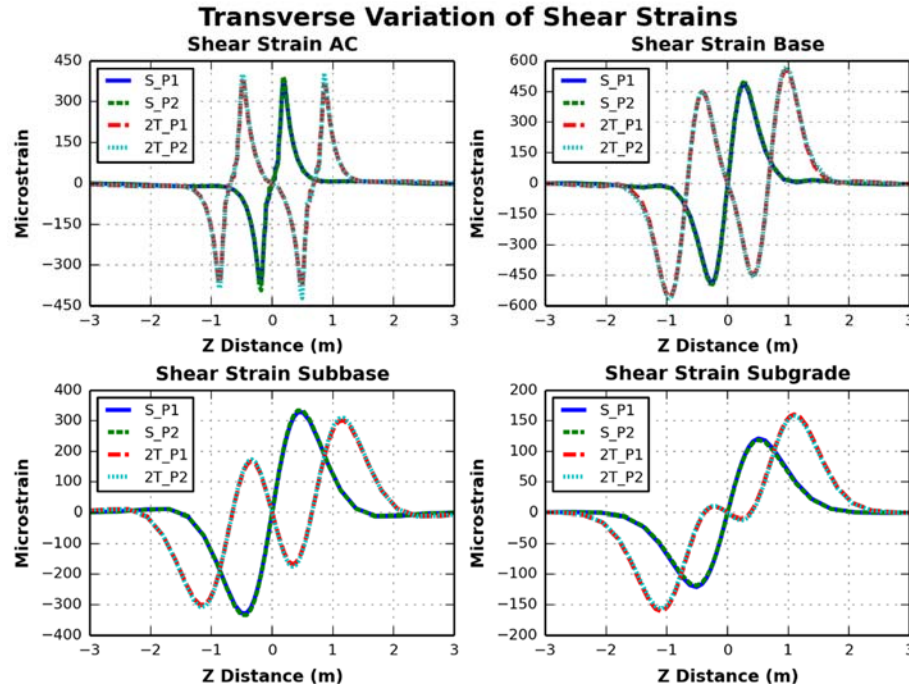


Figure 11. Variation of shear strains along the direction perpendicular to traffic.

ACKNOWLEDGEMENT

This research was supported by the 2013-2014 Graduate Research Award Program on Public Sector - Aviation Issues from the Airport Cooperative Research Program. The authors would like to acknowledge the feedback and input of the review team members Randy Berg of the Salk Lake City Department of Airports and Vivek Khanna of the Oklahoma Aeronautics Commission. The help of Lawrence Goldstein, program coordinator, is also greatly appreciated. Finally, the authors are indebted to Navneet Garg of Federal Aviation Administration, who provided material properties information.

REFERENCES

1. Federal Aviation Administration, "Airport Pavement Design and Evaluation," Advisory Circular AC 150/5320-6E, 2009.
2. Federal Aviation Administration, "National Airport Pavement Test Facility," 2013. [Online]. Available: <http://www.airporttech.tc.faa.gov/naptf/>.
3. Gomez-Ramirez, F.M., and Thompson, M. R., "Aircraft Multiple Wheel Gear Load Interaction Effects on Airport Flexible Pavement Responses," Proceedings of the Advancing Airfield Pavements Conference. Chicago, Illinois, USA, August 5 – 8, 2001.
4. Thompson, M.R., and Garg, N., "Wheel Load Interaction: Critical Airport Pavement Responses," Technical Report COE No. 7, Center of Excellence for Airport Pavement Research, Department of Civil and Environmental Engineering, University of Illinois at Urbana-Champaign, Urbana, Illinois, July 1999.

5. Gopalakrishnan, K., and Thompson, M.R., "Assessing Damage to Airport Pavement Structure due to Complex Gear Loads," *Journal of Transportation Engineering*, ASCE, Vol. 132, No. 11, pp. 888–897, 2006.
6. Gopalakrishnan, K., and Thompson, M.R., "Severity Effects of Dual-Tandem and Dual-Tridem Repeated Heavier Aircraft Gear Loading on Pavement Rutting Performance," *International Journal of Pavement Engineering*, Vol. 7, No. 3, pp. 179–190, 2006.
7. Kim, M., and Tutumluer, E., "Multiple Wheel-Load Interaction in Flexible Pavements," *Transportation Research Record: Journal of the Transportation Research Board*, Vol. 2068, pp. 49–60, 2008.
8. Zhao, H., Ling, J., and Yao, Z., "Study on Pavement Superposition Effects under Multiple Aircraft Tires," Proceedings of the *GeoShanghai 2010 International Conference*, Shanghai, China, June 3 – 10, 2010.
9. Elseifi, M.A., Al-Qadi, I.L., and Yoo, P.J., "Viscoelastic Modeling and Field Validation of Flexible Pavements," *Journal of Engineering Mechanics*, ASCE, Vol. 132, No. 2, pp. 172–178, 2006.
10. Al-Qadi, I.L., Wang, H., and Tutumluer, E., "Dynamic Analysis of Thin Asphalt Pavements by Using Cross-Anisotropic Stress-Dependent Properties for Granular Layer," *Transportation Research Record: Journal of the Transportation Research Board*, Vol. 2154, pp. 156–163, 2010.
11. Wang, H., and Al-Qadi, I.L., "Importance of Nonlinear Anisotropic Modeling of Granular Base for Predicting Maximum Viscoelastic Pavement Responses under Moving Vehicular Loading," *Journal of Engineering Mechanics*, ASCE, Vol. 139, No. 1, pp. 29–38, 2013.
12. Al-Qadi, I.L., and Yoo, P.J., "Effect of Surface Tangential Contact Stresses on Flexible Pavement Response," *Journal of the Association of Asphalt Paving Technologists*, Vol. 76, pp. 663–692, 2007.
13. Wang, H., and Al-Qadi, I.L., "Combined Effect of Moving Wheel Loading and Three-Dimensional Contact Stresses on Perpetual Pavement Responses," *Transportation Research Record: Journal of the Transportation Research Board*, Vol. 2095, pp. 53–61, 2009.
14. Yoo, P.J., Al-Qadi, I.L., Elseifi, M.A., and Janajreh, I., "Flexible Pavement Responses to Different Loading Amplitudes Considering Layer Interface Condition and Lateral Shear Forces," *International Journal of Pavement Engineering*, Vol. 7, No. 1, pp. 73–86, 2006.
15. Wang, H., and Al-Qadi, I.L., "Impact of Non-Uniform Aircraft Tire Pressure on Airfield Pavement Responses," Proceeding of the Transportation and Development Institute Congress, ASCE, Chicago, Illinois, USA, March 13 – 16, 2011.
16. Yoo, P.J., and Al-Qadi, I.L., "Effect of Transient Dynamic Loading on Flexible Pavements," *Transportation Research Record: Journal of the Transportation Research Board*, Vol. 1990, pp. 129–140, 2007.
17. Hjelmstad, K.D., Qiuhai, Z., and Kim, J., "Elastic Pavement Analysis Using Infinite Elements," *Transportation Research Record: Journal of the Transportation Research Board*, Vol. 1568, pp. 72–76, 1997.
18. Airbus, "A380 Airplane Characteristics for Airport Planning," Airbus S.A.S., France, Tech. Rep., 2005.
19. Hernandez, J. A., Gamez, A., Al-Qadi, I. L., and De Beer, M. "Introducing an Analytical Approach for Predicting 3D Tire-Pavement Contact Load," Proceeding of the Transportation Research Board 93rd Annual Meeting, Washington, D.C., USA, January 12 – 16, 2014.